PHILIPPINE ENGINEERING JOURNAL
PEJ 2013; Vol. 34, No. 2: 1-22

# A NUMERICAL INVESTIGATION INTO THE PERFORMANCE AND AERODYNAMICS OF A VERTICAL AXIS WIND TURBINE

**Louis Angelo Danao**
Department of Mechanical Engineering
University of the Philippines
Diliman, Quezon City, Philippines

## ABSTRACT

*Numerical simulations were carried out to investigate the performance of a wind tunnel scale vertical axis wind turbine (VAWT). Steady wind simulations at* $U_\infty$ *= 7m/s have shown that at the low* $\lambda$ *range, there is a distinct negative trough in the power coefficient (CP) that is drag–dominated and consistent to experimental results. Minimum CP is –0.04 at* $\lambda = 2$ *while maximum CP is 0.33 at* $\lambda^* = 4.5$*. A closer inspection of two* $\lambda$*'s reveals that at* $\lambda = 2$*, the blades experience stalled flow initially from a separation bubble forming at* $\theta = 60°$ *with subsequent shedding of vortices. Reattachment occurs very much delayed beyond halfway of the rotation. The same delayed reattachment is observed in the downwind with partial stall still visible at* $\theta = 330°$*. At* $\lambda = 4$*, blade stall is only observed in the second quadrant of rotation with the deepest stall seen at* $\theta = 130°$*. High values of positive blade torque* $T_b$ *reaching 1N·m are predicted in the upwind while most of the downwind region from* $\theta = 190°$ *to* $\theta = 340°$ *also produce positive performance that contribute to the overall positive CP of just below 0.3.*

**Keywords:** *computational fluid dynamics, vertical axis wind turbine, aerodynamics*

## 1. INTRODUCTION

The ill–effects of fossil fuel consumption has increased in the recent years as evidenced by the occurrence of more severe and prevalent climatic disturbances [1]. As such, the reduction of carbon emissions has been pushed through the use of alternative and sustainable technologies especially in the production of energy. Alternative sources to fossil fuels such as tidal, solar, biomass, and wind have gained increased attention in the past decades with wind as one of the major contributors in energy generation in the U.K. [2]. Wind has been the leading renewable technology for electricity generation with 45% of the total 2011 renewable production. Despite this figure, the consumption of electricity from renewable sources is very low at 9.4% [3]. To encourage the wider adoption of this renewable resource, further research is necessary to increase the understanding of energy production through wind.

---

Correspondence to: Louis Angelo Danao, Dept. of Mechanical Engineering, University of the Philippines, Diliman, Quezon City. Email: louisdanao@coe.upd.edu.ph.

*Received: February 6, 2013*
*Accepted: May 21, 2013*

There are two general categories of wind turbines: drag machines (Figure 1a) and lift machines (Figure 1b & c). Drag machines generate forces through the creation of large separated flows, causing high levels of pressure difference between the two sides of a blade. Typically, blade speeds are much lower than the wind speed. Traditionally, these devices are used in water pumping. Lift machines generate thrust by forcing the wind to follow a curved path as it passes about a rounded object. It is the turning of the fluid that creates the forces on the surface of the object, typically of an aerofoil profile. Blade speeds are most often greater than the wind speed and far exceeds what is possible in drag machines.

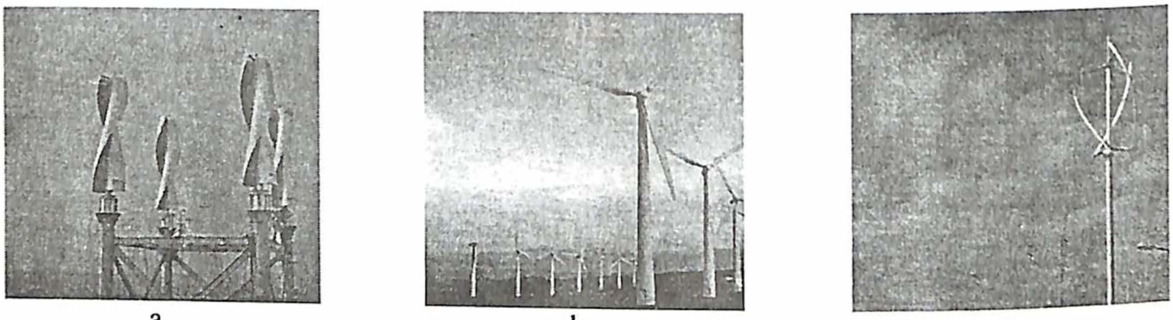
a. b. c.

**Figure 1.** Examples of wind turbines: a) drag VAWT[1], b) lift HAWT[2], c) lift VAWT[3].

Lift machines can be classified further into two configurations: horizontal axis wind turbines or HAWT (Figure 1b) and vertical axis wind turbines or VAWT (Figure 1c). HAWTs are well–established and have mature technology as they have received significant research and development work over the decades. This makes them the preferred configuration in all large scale wind farm installations. VAWTs on the other hand have only just received attention due to their perceived potential in small scale energy generation. VAWT operation involves complex aerodynamic and structural aspects that make their understanding and optimisation difficult, a possible reason why they are less favoured than their horizontal counterparts.

There are several points of contention on the use of VAWTs over HAWTs. The key point that prevails is the generally perceived superior performance of HAWTs over VAWTs. Nevertheless, VAWTs present a number of potential advantages over HAWTs when it comes to applications in the built environment:

- no need to yaw to the wind thus reducing the efficiency loss when tracking changes in wind direction.
- sound emissions are usually lower as they operate at lower tip speed ratios [4]. This can also reduce structural issues such as vibration that result from high centrifugal forces.
- potentially lower manufacturing costs due to the simplicity of the straight blade shape.
- better performance in skewed flow [5].

---

[1] Oy Windside Production Ltd., http://www.windside.com.

[2] Wikimedia Commons, Creative Commons Attribution 2.0 Generic license.

[3] Quiet Revolution Ltd., http://www.quietrevolution.com.

VAWTs are not without their disadvantages when compared to HAWTs. The most common are:

- lower efficiency due to the additional drag of blades moving against the wind. Moreover, HAWTs are presumably more optimized in their design as a consequence of greater efforts made in research and development.
- less access to stronger winds in higher elevations.
- complex aerodynamics resulting in continuously fluctuating blade loading during operation and therefore a lower fatigue life cycle.
- difficult to implement variable pitch without complicated mechanisms. HAWT blades can be pitched easily to the optimum angle of attack to maximize energy extraction.

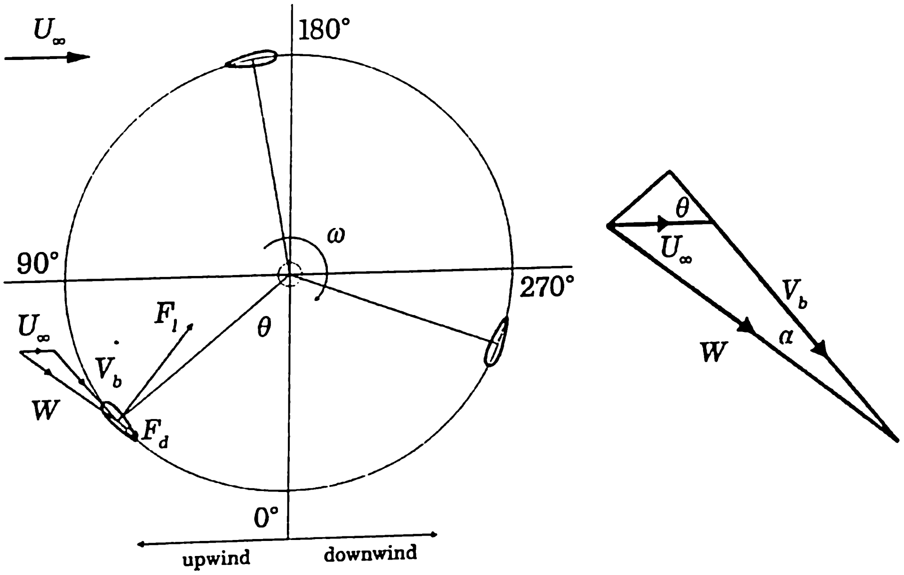

**Figure 2.** An illustration of the vectors on a VAWT blade.

During operation, a VAWT blade experiences cyclic variations in angle of attack $\alpha$. As such, the blade may undergo stalled and unstalled conditions as well as interact with its own wake and that of other blades within one rotation. Figure 2 illustrates the kinematic and kinetic vectors on a VAWT blade. As the VAWT rotates with angular velocity $\omega$ in a flow of wind speed $U_\infty$, the velocity of the wind relative to the blade, W, changes and is given by

$$W = U_\infty + V_b \tag{1}$$

where $V_b = -\omega R$ and R is the radius of the VAWT. This velocity fluctuates from a maximum of $(\lambda + 1)U_\infty$ to a minimum of $(\lambda - 1)U_\infty$, where $\lambda$ is the tip speed ratio. At the same time, the angle of attack $\alpha$ also varies periodically between positive and negative values. The magnitudes of the relative velocity and the angle of attack are given by

$$W = U_\infty\sqrt{1+2\lambda\cos\theta+\lambda^2} \tag{2}$$

$$\alpha = \tan^{-1}\left(\frac{\sin\theta}{\lambda+\cos\theta}\right) \tag{3}$$

where $\theta$ is the azimuth angle and is measured from the vertical Y–axis in the clockwise direction.

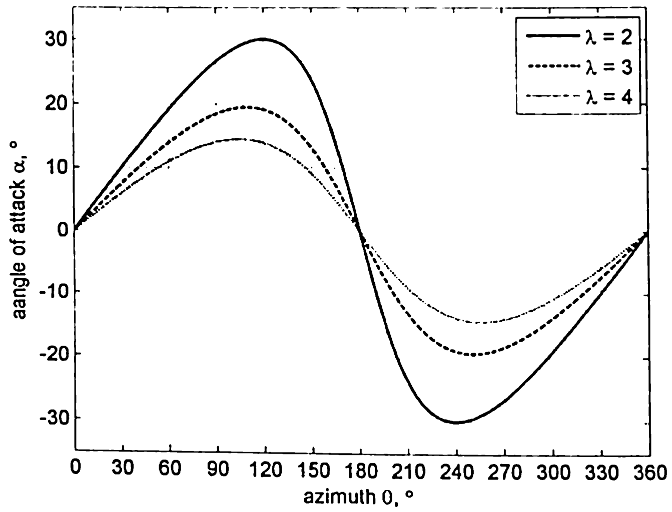

**Figure 3.** Computed angle of attack based on geometric assumption.

The variation of $\alpha$ closely resembles a sine wave as shown in Figure 3. This perceived variation is relative to a reference frame attached to the rotating VAWT with its origin at the VAWT axis. As the tip speed ratio $\lambda$ increases, the skewness of the $\alpha$ variation reduces and the profile comes closer to a sine wave (zero skew).

As a blade rotates, the flow will have a certain incidence on it thereby generating the aerodynamic lift $F_l$ and drag $F_d$ (Figure 2). Both of these forces will have components along the tangential and normal directions. The normal components do not influence the energy generation of the rotor. However, they are a key factor when it comes to structural considerations. The tangential components are the primary driving forces that dictate the performance of the VAWT and give rise to the instantaneous blade torque $T_b$:

$$T_b = (F_l\sin\alpha + F_d\cos\alpha)R \tag{4}$$

There is also the aerodynamic moment about the blade, whose contribution to the overall torque is dependent on where the blade is mounted chord–wise. This is usually small and may be neglected when the mounting point is within the general area of the aerodynamic centre of the profile. Given that a VAWT will likely have more than one blade, the instantaneous rotor power $P_B$ is computed as

$$P_B = N\omega T_b \tag{5}$$

$$P_w = \frac{1}{2}\rho A U_\infty^3 \tag{6}$$

$$CP = \frac{P_B}{P_w} \tag{7}$$

where N is the number of blades. The instantaneous wind power $P_w$ is a function of the VAWT swept area $A = 2RL$ (where L is the blade length), the air density ρ, and the free stream wind speed $U_\infty$ (Eq. 6). Finally, the instantaneous power coefficient CP is the ratio of $P_B$ and $P_w$ (Eq. 7).

In steady wind conditions, the VAWT CP is normally computed by averaging the instantaneous blade torque over one rotor cycle thus making the CP independent of azimuth position and giving a single–valued metric of the VAWT performance.

## 2. CFD SOLVER

The CFD package, Ansys Fluent 13.0, was used for all the simulations performed in this study. The code uses the finite volume method to solve the governing equations for fluids. More specifically in this project the incompressible, unsteady Reynolds Averaged Navier-Stokes (URANS) equations are solved for the entire flow domain. The coupled pressure–based solver was selected with a second order implicit transient formulation for improved accuracy. All solution variables were solved via second order upwind discretisation scheme since most of the flow can be assumed to be not in line with the mesh [6].

The entire domain was initialised using the inlet conditions that were pre–determined to provide a matching turbulence intensity decay that was observed in VAWT experiments conducted in the University of Sheffield wind tunnel facility. The inlet turbulence intensity was set to Tu = 8% with a turbulence viscosity ratio of $\mu_t/\mu = 14$. The Tu decay in the numerical model is very close to the observed decay in the experiment as shown in Figure 4.

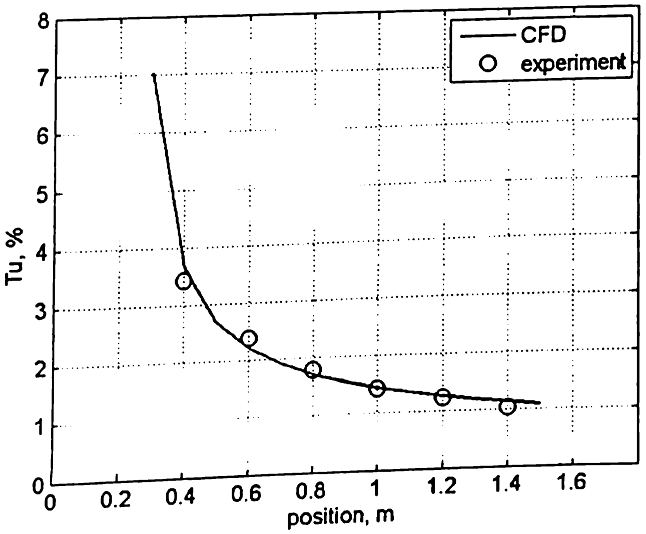

**Figure 4.** Comparison of turbulent intensity decay between CFD and experiments (x = 0: test section inlet).

## 3. NUMERICAL MODEL OF THE WIND TUNNEL VAWT

A two–dimensional CFD model was used to represent the VAWT and the wind tunnel domain. This was based on the review of relevant literature [7-19] that has shown that a 2D model is sufficient in revealing the factors that influence the performance and majority of flow physics that surround the VAWT. The contributions of blade end effects and blade–support arm junction effects are neglected but deemed acceptable since these can be considered as secondary. Two dimensional VAWT models are essentially VAWTs with infinite aspect ratio blades. The effect of blade aspect ratio (AR) comes in the form of shifting the CP curve upwards and to the right as AR increases [20], but the general shape is maintained. Full 3D models were tested using coarse meshes but due to their immense computational time requirements, were eventually shelved. The complexity, as well as the computational expense for a full three dimensional model cannot be justified by the additional insight that such a model can offer.

The domain mesh was created where the aerofoil coordinates of a NACA022 profile were imported to define the blade shape. The surrounding geometry was defined based on studies of the extents of the boundaries that are detailed in later sections. There is an inner circular rotating domain connected to a stationary rectangular domain via a sliding interface boundary condition that conserves both mass and momentum. No–slip boundaries are set to represent the wind tunnel walls while a velocity inlet and a pressure outlet are used for the test section inlet and outlet, respectively. The rotation of the inner domain relative to the outer domain is prescribed within the solver that implements the algorithm for the sliding mesh technique. Care is taken such that tolerance between meshes in the interface region is kept low to avoid excessive numerical diffusion.

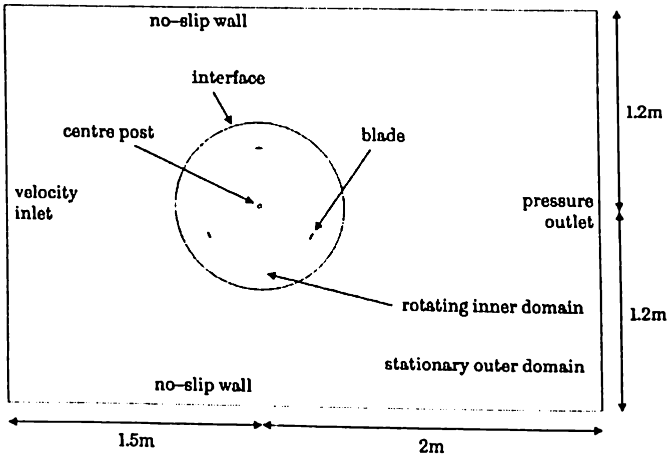

**Figure 5.** An illustration of the 2D numerical domain.

Each blade surface was meshed with 300 nodes and clustering in the leading and trailing edges was implemented to provide the required refinement in regions where high gradients in pressure and flow were expected. A node density study was performed to determine the appropriate number of surface nodes (Figure 6). The O–type mesh was adapted for the model, where a boundary layer was inflated from the blade surface (Figure 7a). The motivation behind using the O–type mesh instead of the conventional C–type used in aerofoil studies was primarily because the expected wake is not fixed on a specific path relative to the blade but rather varying greatly in direction swaying from one side to another side. The use of a C–type mesh would not be beneficial as the tail of the wake from the blade will not always fall within the refined tail mesh. The first cell height used was such that the $y^+$ values from the flow solutions did not exceed 1, the limit of the turbulence model that was chosen for the simulations. To ensure proper boundary layer modelling, the growth rate of the inflation was set to 1.1 to give a minimum of 30 layers within the boundary layer, after which a larger growth rate of 1.15 was implemented. Beyond the blade surface of about a chord width, the rotating inner domain mesh was generated such that the maximum edge length of the cells did not exceed 0.5c within the VAWT domain (Figure 7b). This was adapted to minimize the dissipation of the turbulent structures generated by the blades in the upwind region that may interact with the other blades in downwind region. A smoothing algorithm in the meshing software was used to reduce the angle skewness of the cells such that the maximum was observed to be less than 0.6.

To reduce computation time, the outer domain was coarsely meshed with a rough maximum edge length of the cells set to c (Figure 8). This dissipated the high gradients in the wake, such as shed vortices, but the general velocity deficit was still captured. The distance of the velocity inlet boundary from the VAWT axis was set to 1.5m, 0.3m short of the actual 1.8m in the experiment setup. This was not considered an issue since the modelled turbulence intensity decay in the simulations matched that of the experiments and is thought to be much more important.

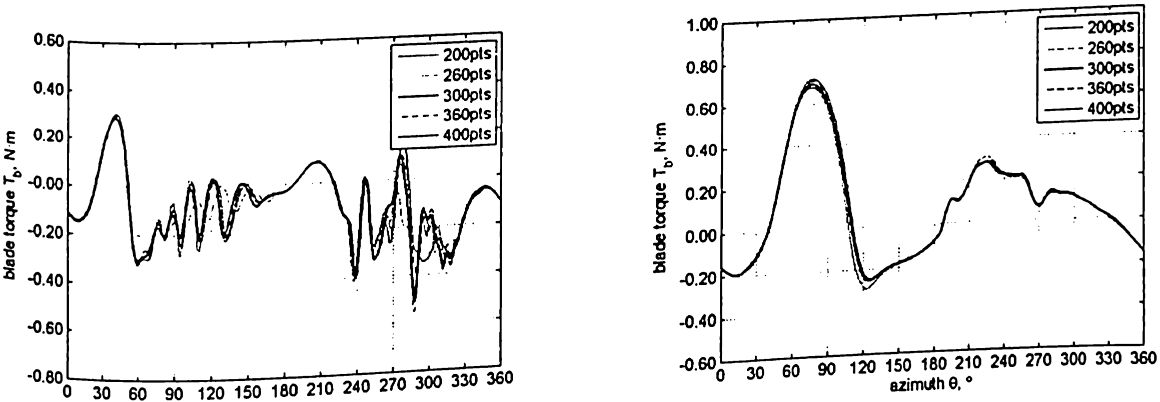

b.

a.

Figure 6. Blade torque for node density study: a) λ = 2, b) λ = 4.

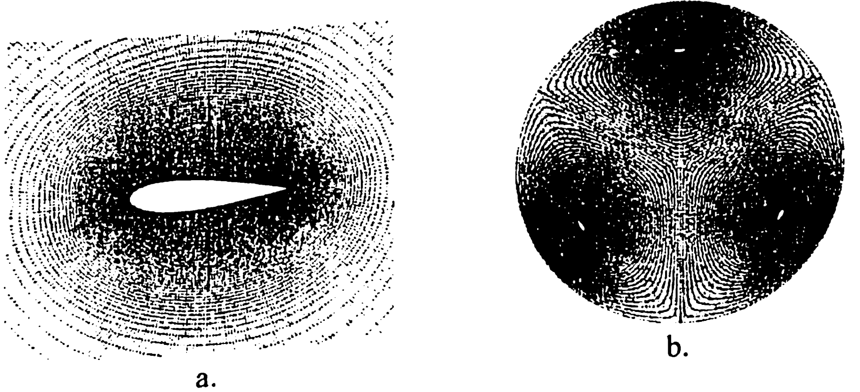

b.

a.

Figure 7. The rotating inner domain mesh: a) the near–blade mesh, b) the full inner domain mesh.

An outlet distance study was conducted to investigate the effects of wake development on the performance of the VAWT (Figure 9a). The pressure outlet boundary was set to $d_o$ = 2m from the VAWT axis. This has been selected as a distance between the actual test section outlet of 1.2m and the position of the wind tunnel fan of about 3m. In the actual wind tunnel setup, the test section outlet was fitted with a steel matting grid of the same wire thickness and mesh size as the turbulence grid in the inlet. This will have had a definite effect on the developed wake of the VAWT, breaking up the large vortex structures generated from the blades. There is also the presence of the shutter flaps, which is considered to influence the destruction of the shed vortices. As such, a long fluid domain behind the VAWT was deemed unnecessary from a numerical standpoint since full wake development was not one of the objectives of the study.

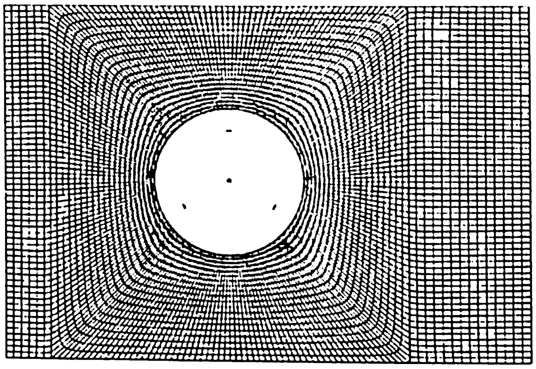

Figure 8. The stationary outer domain mesh of the numerical model.

A wall distance study was carried out to examine the effects of blockage in the 2D simulations (Figure 9b). The side wall distance was set to $d_s$ = 1.2m from the VAWT axis. This is double the actual wind tunnel wall distance of 0.6m. The blockage of the 2D numerical model matches that of the 3D wind tunnel model and is equal to 0.29. Since the study is mainly focused on the aerodynamics of the VAWT in unsteady wind conditions within a wind tunnel domain, blockage was not a primary consideration in the simulations since no reference to actual field test data is made.

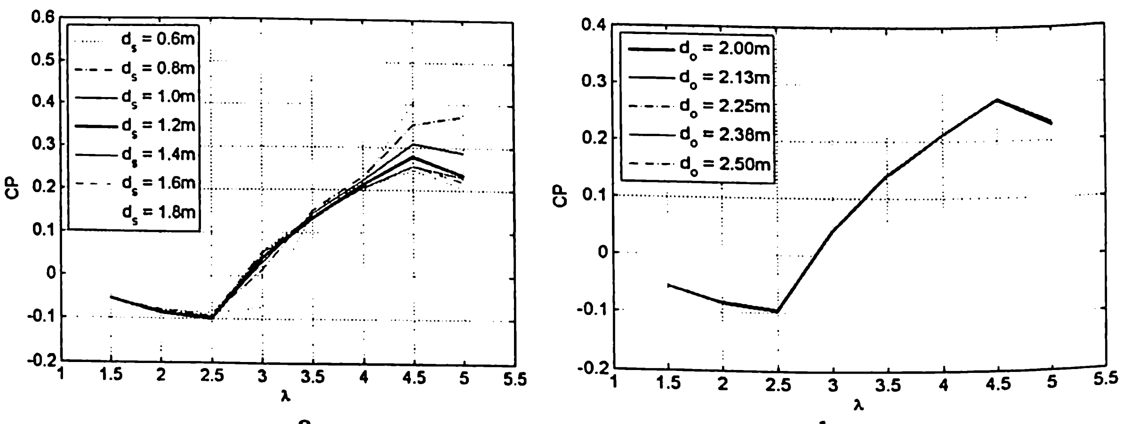

a. b.

Figure 9. Domain size study results for the 2D numerical model: a) side wall distance, b) domain length.

Time step convergence was monitored for all conserved variables and it was observed that acceptable levels of residuals (less than 1 × $10^{-6}$) were attained after 6 rotations of the VAWT. This meant that periodic convergence was also achieved. The blade torque $T_b$ monitored all through 10 rotations is shown in Figure 10. After the sixth rotation, the peaks of the upwind torque for cycles 7 through 10 are level and the downwind ripple match closely. The difference in average torque between cycle 7 and cycle 10 is around 0.5%

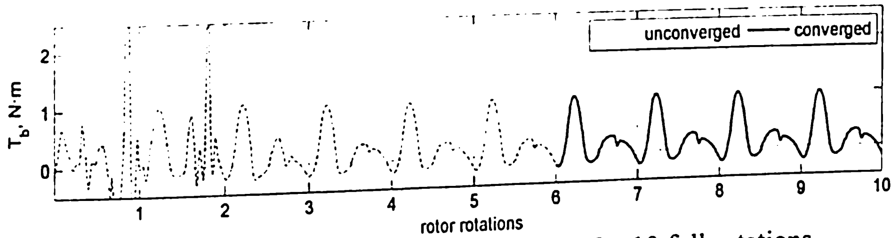

**Figure 10.** Blade torque ripple of one blade for 10 full rotations.

Sufficient temporal resolution is necessary to ensure proper unsteady simulation of the VAWT. Different time step sizes Δt that are equivalent to specific rotational displacements along the azimuth were tested. The largest Δt used was equal to a $\Delta t = 1°\omega^{-1}$ (time for one degree equivalent rotation) and was subsequently halved twice over to get $\Delta t = 0.5°\omega^{-1}$ and $\Delta t = 0.25°\omega^{-1}$. All three Δt's were tested at $\lambda = 2$ and $\lambda = 4$. Results for both λ are presented in Figure 11. It is clear that there is a delay in the torque ripple for the coarsest $\Delta t = 1°\omega^{-1}$ for $\lambda = 2$ while the two finer Δt's are in good agreement especially in the upwind. A small difference in predicted magnitude of $T_b$ between $\Delta t = 0.5°\omega^{-1}$ and $0.25°\omega^{-1}$ is seen from $\theta = 280°$ to $\theta = 330°$ but the peaks and troughs are still in sync. In terms of CP, there is negligible difference between the three Δt's with a maximum ΔCP of only 0.003. A similar agreement between the three Δt's is observed at $\lambda = 4$ with the maximum ΔCP of 0.003 as well. There is very little variation between the three cases with the only noticeable difference in the torque ripple from $\theta = 260°$ to $\theta = 290°$. The upwind is accurately predicted by the three Δt's with all capturing the maximum $T_b$ around $\theta = 80°$. The maximum $T_b$ in the downwind is also properly predicted by all Δt's at $\theta = 240°$. Since time accurate simulations is required for this study, the chosen time step size was $\Delta t = 0.5°\omega^{-1}$ so that the vortex shedding at $\lambda = 2$ is correctly modelled and was adapted for the remaining runs.

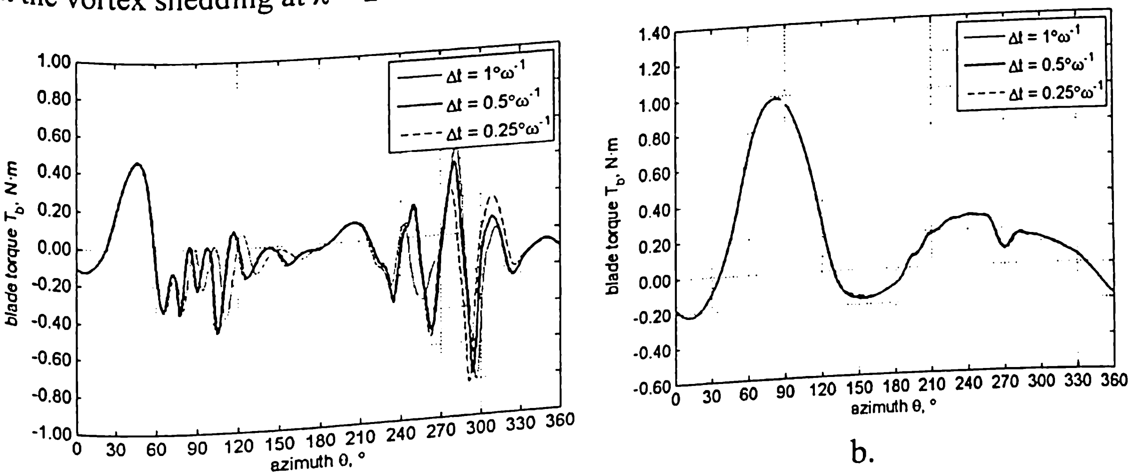

a.

b.

**Figure 11.** Time step size study results: a) $\lambda = 2$, b) $\lambda = 4$.

## 4. VALIDATION OF CFD MODEL

The numerical model developed was checked against experimental data to assess its capability of correctly simulating VAWT flow physics. The validation is not considered exact, since the CFD model is 2D, while the actual problem is 3D. Nevertheless, a good 2D CFD model will provide substantial insight into the factors driving the performance of the VAWT and a means of checking the model's accuracy in capturing the details of the problem is presented below.

### *4.1 Power Coefficient*

The first aspect of the model validation is the comparison of the predicted VAWT performance over a wide range of operating speeds. Both the fully turbulent k–ω SST and the Transition SST models were tested against the experimentally derived CP [21]. The steady wind speed chosen was 7m/s and the simulations were run at different tip speed ratios from λ = 1.5 up to λ = 5 in increments of 0.5. It can be seen from Figure 12 that both 2D models over–predict CP starting from λ = 2 all the way up to λ = 5. Maximum CP for the fully turbulent model is 0.35 at λ = 4 while the Transition SST model predicts maximum CP = 0.33 at λ = 4.5. The maximum CP for the fully turbulent model occurs at the same λ as that of the experiments. There is a gap in the predicted CP's between the two CFD models from λ = 3 to λ = 4.5 where the fully turbulent model over–predicts the CP much more than the Transition SST model. A convergence of the curves is seen from λ = 1.5 to λ = 3 and also from λ = 4.5 to λ = 5. Higher λ's show the greatest over–prediction of the CFD models from experiments. This may be due to the effects of finite blade span where the reduction in aspect ratio as seen by McIntosh [20] cause a substantial drop in CP at high λ versus the small drop in CP at low λ.

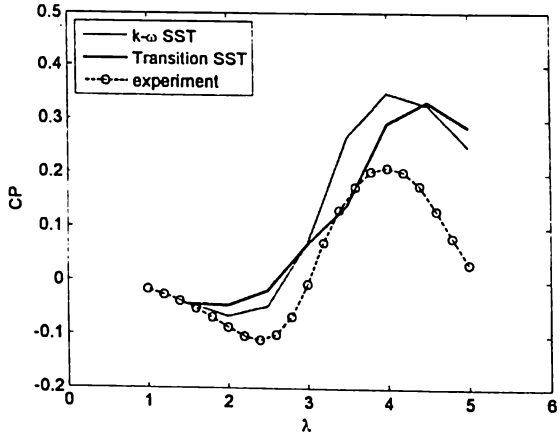

Figure 12. Steady CP curves at 7m/s.

The gap in predicted CP was expected since the 2D model does not account for finite blade span as well as for blade–support arm junction effects and support arm drag that are present in the actual setup. The results are consistent to published data by Raciti Castelli et al [15], Howell et al [13] and Edwards et al [11] where 2D CP is over–predicted over the entire range of λ. Raciti Castelli et al compared their 2D simulations to wind tunnel experiments and argued that the difference is due to blockage effects that increase the flow velocities near the blades to much higher values than the unperturbed flow at the inlet. Howell et al show an improved match between 3D CFD and experiments. Edwards et al attribute the difference in predicted CP to finite blade span and blade–support arm junction effects.

Overall, the general trend of the predicted CP matches well with the experimental data. There is an observed negative trough at the low λ which rapidly rises and reaches maximum values near the experiment maximum at λ = 4 after which a rapid drop in CP is seen. In terms of shape, the fully turbulent model results show a smoother curve and better agreement to experiments while the Transition SST model results do not form a smooth curve and predict maximum CP at a higher λ.

### *4.2 Visualisations*

The second aspect of validation is the comparison of flow visualisations between CFD and particle image velocimetry (PIV) data [21]. This part is an important step since the behaviour of the flow around the VAWT blades add significant insight as to why the CP varies as it does at different operating conditions. The flow physics at two λ are inspected and an assessment of the most appropriate turbulence model is performed based on the accuracy of the predicted stalling and reattachment of the flow on the blades as they go around the VAWT.

#### *Flowfield at λ = 2*

Figure 13 shows the vorticity plots for the upwind at λ = 2. At the start of the rotation, both turbulence models clearly predicts fully attached flow. There is an observed wake (green contour) seen on the lower left portion of each CFD image at θ = 10° that is also visible in the PIV image. This is the wake of the preceding blade already at θ = 130°. Flow continues to be attached until θ = 60° where both the Transition SST model and PIV reveal a bubble that is forming on the suction surface of the blade. The fully turbulent k–ω SST predicts the same formation of a separation bubble 10° later at θ = 70°. This delay has a significant effect on the blade torque since this can mean extended generation of lift that may positively affect the predicted performance of the VAWT.

As seen in the PIV at θ = 70° the separation bubble has formed into a dynamic stall vortex and has already been detached from the blade surface. This is properly captured by the Transition SST model. However, the fully turbulent model still predicts the vortex to be on the blade surface. This delay in the formation and detachment of the dynamic stall vortex affects the shedding of the subsequent pairs of leading edge and trailing edge vortices and is evident in the presence of a trailing edge vortex in the field of view (FOV) of the fully turbulent model at θ = 140° but is not seen on both the Transition SST model and PIV.

The downwind (not shown for brevity) shows better agreement between the two CFD models when it comes to the scale and timing of the shed vortices although slightly smaller when compared to the PIV. The flow reattachment is seen to have started earlier in the Transition SST model as the stall is significantly shallower at θ = 280° as compared to the fully turbulent model and PIV. This may, in part, explain the higher predicted CP at this λ. Overall, the timing and depth of stall in the upwind for the Transition SST model matches the PIV quite well while the reattachment of the flow in the downwind is better captured by the fully turbulent model.

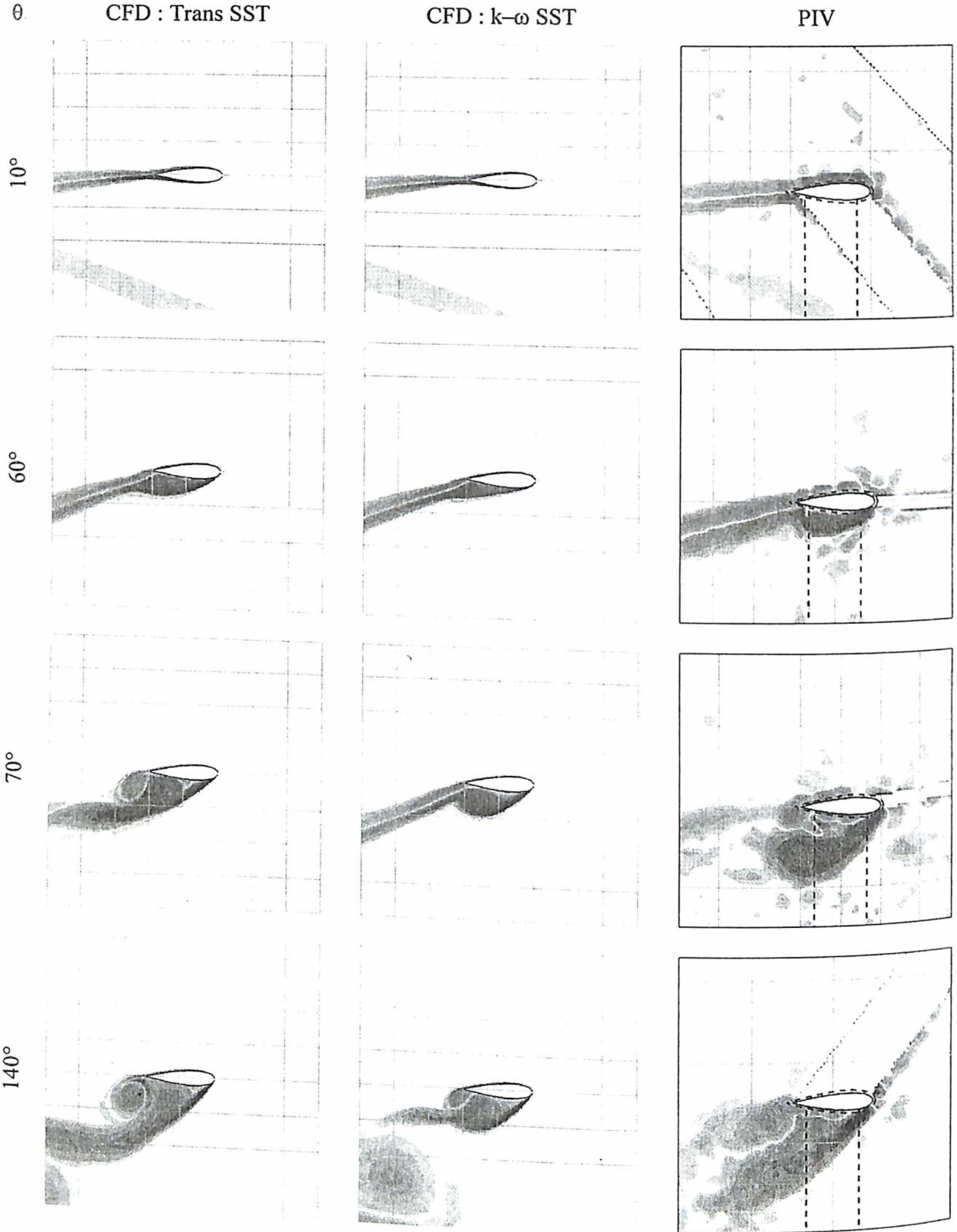

Figure 13. Flow visualisations of vorticity in the upwind for λ = 2.

### *Flowfield at $\lambda = 4$*

Flow visualisations for $\lambda = 4$ are presented in Figure 14. For the most part, the flow is attached to the blade. The wake of a previous blade (green band) is visible in the lower portion of the images at $\theta = 40°$. At $\theta = 120°$, the Transition SST model shows an almost full stall on the suction surface while very light stall is seen in the fully turbulent model and PIV. Ten degrees later at $\theta = 130°$, the Transition SST model shows a deep full stall that is consistent to the PIV while partial stall is still observed in the fully turbulent model. The delay in stalling will have increased the positive performance of the fully turbulent model and pushed the CP to higher values as seen in Figure 12. At $\theta = 170°$, the fully turbulent model shows full reattachment of the flow while the PIV still shows partial separation from mid–chord to trailing edge. The Transition SST model is still stalled but to a lesser degree and produces a narrower wake when compared to PIV.

Based on the results obtained from both force and flow validation, the Transition SST model was selected as the best model that most accurately captures the flow physics of the VAWT. From the correct prediction of start of stall and the rate and scale of shed vortices at $\lambda = 2$ to the stalling and reattachment of flow at $\lambda = 4$, the Transition SST model better calculates the flow physics versus the k–ω SST model. The predicted positive performance of the Transition SST model is closer to experiments with lower values of CP versus the k–ω SST model. All further simulations conducted will use the Transition SST model.

## 5. STEADY WIND PERFORMANCE

The performance of the VAWT was investigated under steady wind conditions of $U_\infty = 7$m/s and was validated against experimental data. Following the validation is a closer inspection of the numerical data to give a better understanding of the behaviour in VAWT performance across a wide operating range. This is discussed in the following sections.

### *5.1 Power Coefficient*

The variation of CP versus $\lambda$ is repeated in Figure 15. There is a marked difference between the predicted CP and the actual CP especially in the power producing region ($4 < \lambda < 5$). The maximum measured CP is 0.21 at $\lambda = 4$ while the maximum predicted CP is 0.33 at $\lambda = 4.5$, a shift of the power curve upwards and to the right is explained by the effects of having infinite AR in the 2D numerical model. Low AR, as is the case of the actual experimental VAWT, increases the induced drag due to tip effects in proportion to the positive performance of the blades [20]. The negative trough at low $\lambda$ is still present but is also over predicted by the numerical model from the experiment minimum CP of $-0.11$ at $\lambda = 2.4$ to the predicted $-0.04$ at $\lambda = 2$. The predicted CP does not follow a smooth curve as $\lambda$ increases from $\lambda = 3$ to $\lambda = 4$. There is a slight kink in the CP curve at $\lambda = 3.5$ towards the right which causes it to touch the experimental CP curve. There is no conclusive explanation to this behaviour despite closer inspection of the blade torque curves and flow visualisations across the entire range of $\lambda$.

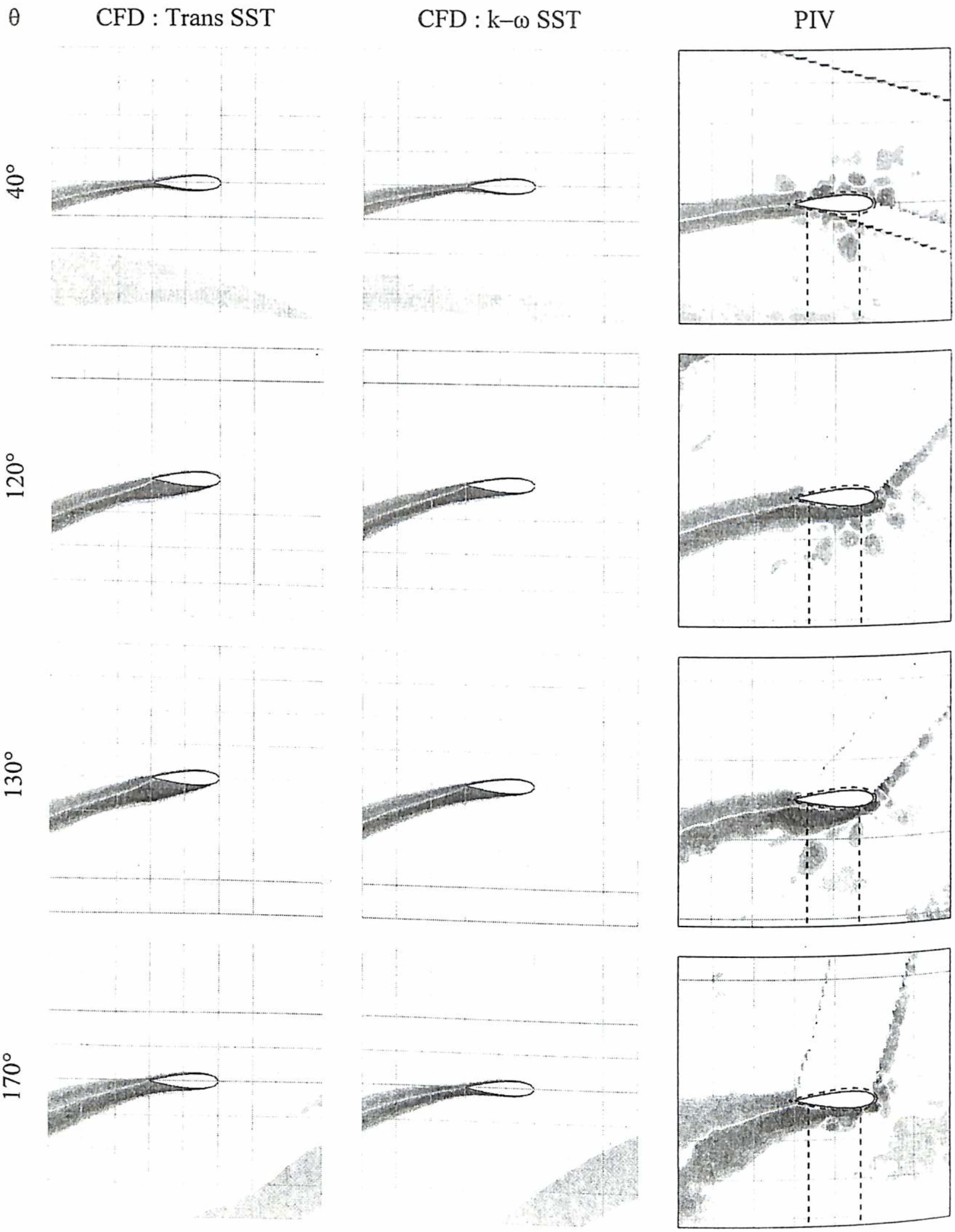

**Figure 14.** Flow visualisations of vorticity in the downwind for λ = 4.

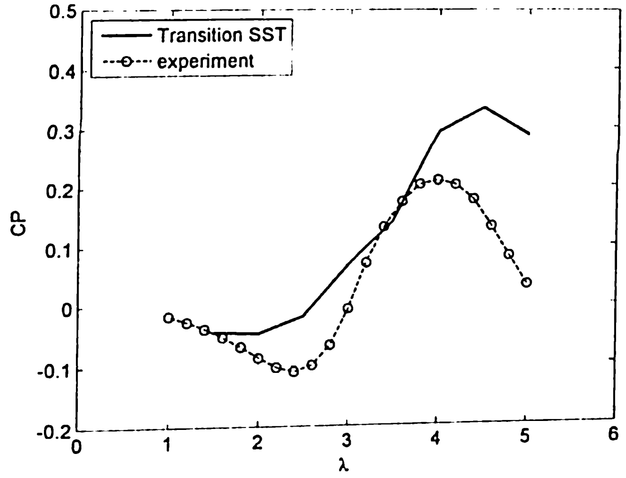

Figure 15. Steady wind performance of the VAWT at U∞ = 7m/s.

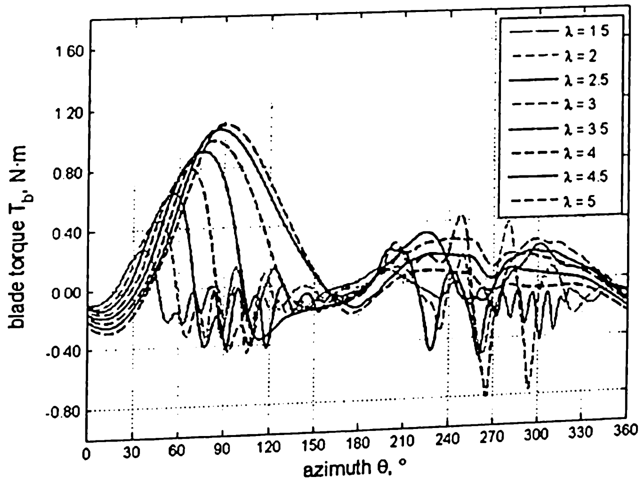

Figure 16. Blade torque curves for one blade at U∞ = 7m/s.

As λ increases from λ = 1.5 to λ = 5, maximum $T_b$ for one full rotation is observed to increase and the stalling in the upwind progressively delayed (Figure 16). Downwind performance is also seen to improve as λ increases from λ = 1.5 to λ = 4 resulting in the steady increase in CP. At λ = 4.5, $T_b$ in the downwind is lower than at λ = 4. However, $T_b$ in the upwind is higher and stays positive longer at λ = 4.5 than at λ = 4 which results in a higher CP at λ = 4.5. Upwind performance is very similar for both λ = 4.5 and λ = 5. The main factor for the lower CP at λ = 5 is the poorer performance in the downwind with negative $T_b$ observed to commence at θ = 258° versus the λ = 4.5 case where $T_b$ dips into the negative region at a much later azimuth of θ = 325°.

The observed differences in the performance of the VAWT at different λ can be explained by analysing the aerodynamic forces on the blade. Traditionally lift and drag coefficients are used as the bases for the assessment of aerofoil performance and this is attempted in the following analysis to further the understanding of VAWT performance using familiar means. Alongside flow visualisations and the CP–λ curve, a complete picture of the VAWT performance can be constructed using detailed comparisons of lift and drag variation as blades go around one full rotation.

Following on from the experimental validation section where two λ are tested, the same is conducted in this analysis. The main reason for testing these two λ is their significant dissimilarity in almost all aspects of performance. In this way, significant differences can be presented for comparison between extreme operating conditions. The two λ tested are λ = 2 and λ = 4. For each simulation, the moment coefficient of one blade is recorded and the final rotation is presented in Figure 17. It can be seen that the upwind performance at λ = 4 is considerably better than at λ = 2 with more than double the maximum $T_b$ predicted at $T_b$ = 0.98N·m. The stalling is also very much delayed in the higher λ while a ripple of the $T_b$ curve is present in the lower λ indicating the shedding of vortices. Much of the blade torque is negative at λ = 2 while the opposite is observed at λ = 4. The predominantly negative torque at λ = 2 explains the negative CP at this λ. Point 1 in the $T_b$ curve of λ = 4 is at θ = 82.5°, the maximum value of $T_b$ for the rotation. At this azimuth in the first quadrant of rotation, the lift is close to maximum at $C_l$ = 0.92, almost double that of the CFD–derived static stall lift of $C_{l,ss}$ = 0.59 at angle of attack $\alpha_{ss}$ = 11° (Figure 18).

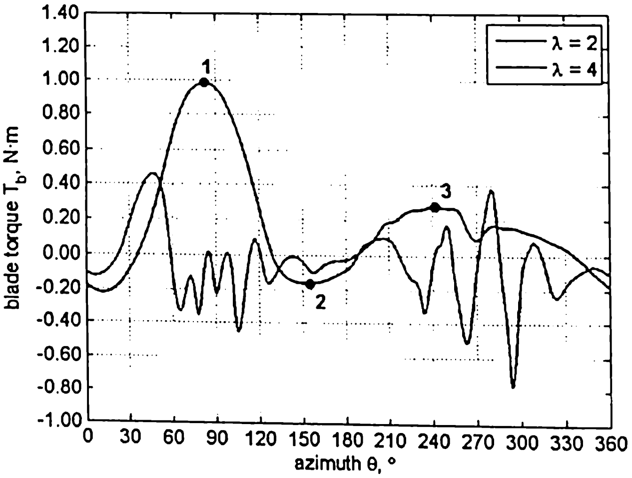

Figure 17. Blade torque curves of two λ cases at U∞ = 7m/s.

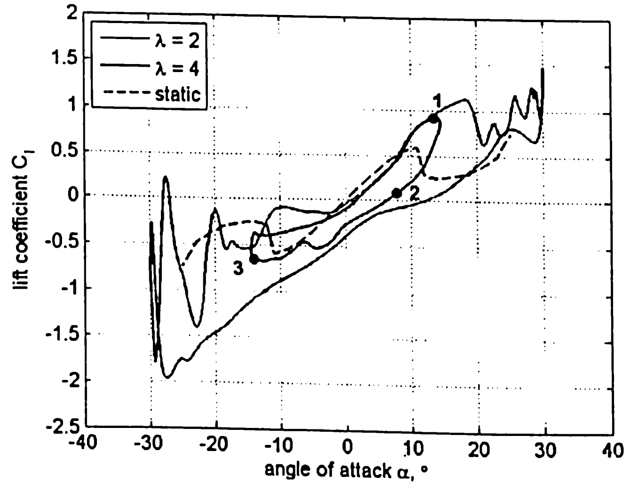

Figure 18. Lift coefficient plot of two λ cases at $U_\infty$ = 7m/s.

The increased lift is due to the dynamic stall effect as the blade moves in a pitching–type motion relative to the flow. Drag at this point is also higher at $C_d = 0.11$, almost double that of the static stall drag of $C_{d,ss} = 0.06$ (Figure 19). These observations are typical of dynamic stall phenomenon [22] and are expected even at this λ since the computed α at point 1 is higher than $\alpha_{ss}$ at 13.5°(Figure 20). The effects of dynamic stall are more evident at $\lambda = 2$ where the maximum lift before stall exceeds that of $\lambda = 4$. Even after stall, lift is still increasing as vortices are shed from the blade up until α reaches maximum at 30° with $C_l$ topping at 1.5. Despite the high lift, $T_b$ is negative because of the overpowering effect of drag which has reached an upwind maximum of $C_d = 0.97$. Even at high values of α, the drag is still more aligned to the tangential direction than the lift, inducing drag dominated performance.

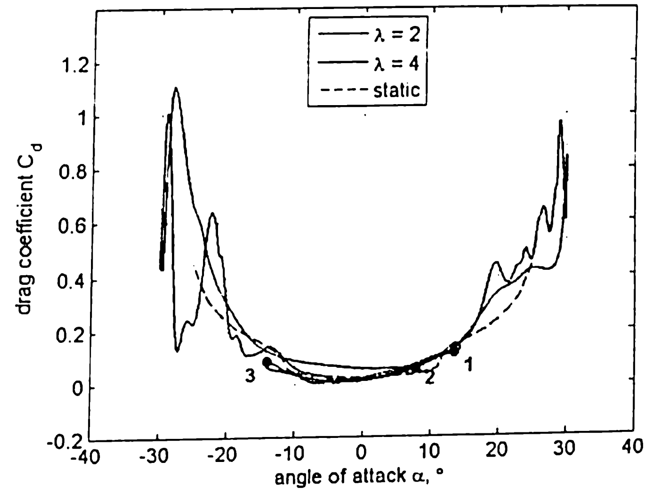

Figure 19. Drag coefficient plot of two λ cases at $U_\infty = 7$m/s.

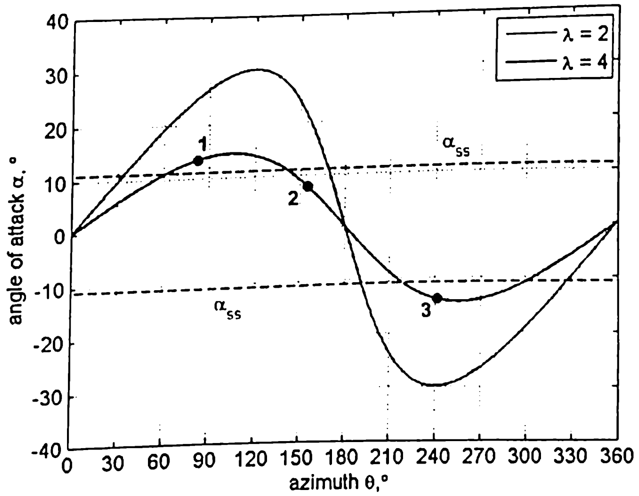

Figure 20. Variation in α of two λ cases at $U_\infty = 7$m/s, $\alpha_{ss}$ is the static stall α.

After point 1, $T_b$ rapidly drops and reaches the negative region as the blade sees stalled flow. The lowest point of the $T_b$ curve in the second quadrant is at $\theta = 155°$ (point 2). The α at this point is 7.8° and while this is not particularly low with static $C_l$ around 0.5, lift on the blade has dramatically dropped to $C_l = 0.08$ with the drag halved at $C_d = 0.06$. The relatively high drag and an almost negligible lift is the main reason why the $T_b$ at this point is negative at –0.16N·m. Just after the third quadrant at $\theta = 241.5°$, maximum $T_b = 0.28$N·m is attained in the downwind at point 3 just before the blade interacts with the wake of the centre post. Although the $\alpha$ at this point is 14° which should bring the blade into dynamic stall, lift is much lower than the upwind maximum at $C_l = 0.66$ while drag is also lower at $C_d = 0.09$. This is not surprising since there is velocity induction in the upwind due to power extraction subsequently lowering the available energy content in the flow.

### *5.2 Flow Visualisations*

A better appreciation of the variation in lift and drag can be attained through the inspection of the flow visualisations as the blade goes around the rotation. Although there are three blades present in the rotor, the symmetry of the rotor allows for a set of images for one blade going around one full rotation to be sufficient in giving a complete picture of the problem. Corresponding torque values plotted in polar coordinates compliment the visualisations to make a concise summary of the performance. This diagram style is adapted for both test cases of $\lambda$.

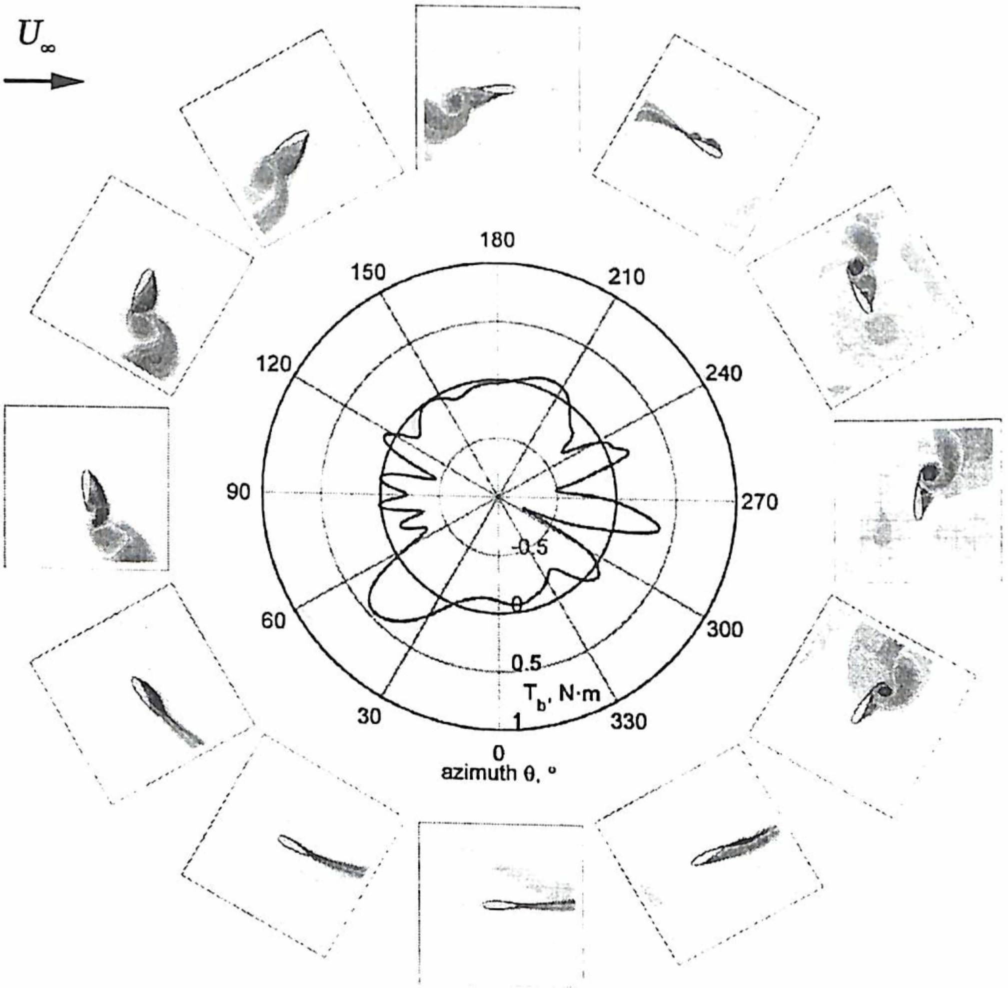

**Figure 21.** Plot showing blade torque and flow field variation with azimuth for steady wind case $U_\infty = 7$m/s at $\lambda = 2$.

*Flowfield at $\lambda = 2$*

The variation of blade torque $T_b$ through one full rotation is plotted in Figure 21 alongside flow visualisations. Large regions of negative torque are visible and huge fluctuations in magnitude agree closely with azimuth positions showing deep stall and vortex shedding. Most of the positive torque in the upwind is produced between $\theta = 30°$ and $\theta = 60°$ while negative values are seen all the way until mid rotation. This poor performance is a consequence of the very steep $\alpha$ that the blade sees inducing the persistent large scale vortex shedding seen. In the downwind, a similar picture is observed with blade scale vortices being shed after $\theta = 210°$ until past $\theta = 300°$. Delayed reattachment occurs at $\theta = 330°$, despite the expected low $\alpha$ at this point in the rotation further lowering the performance.

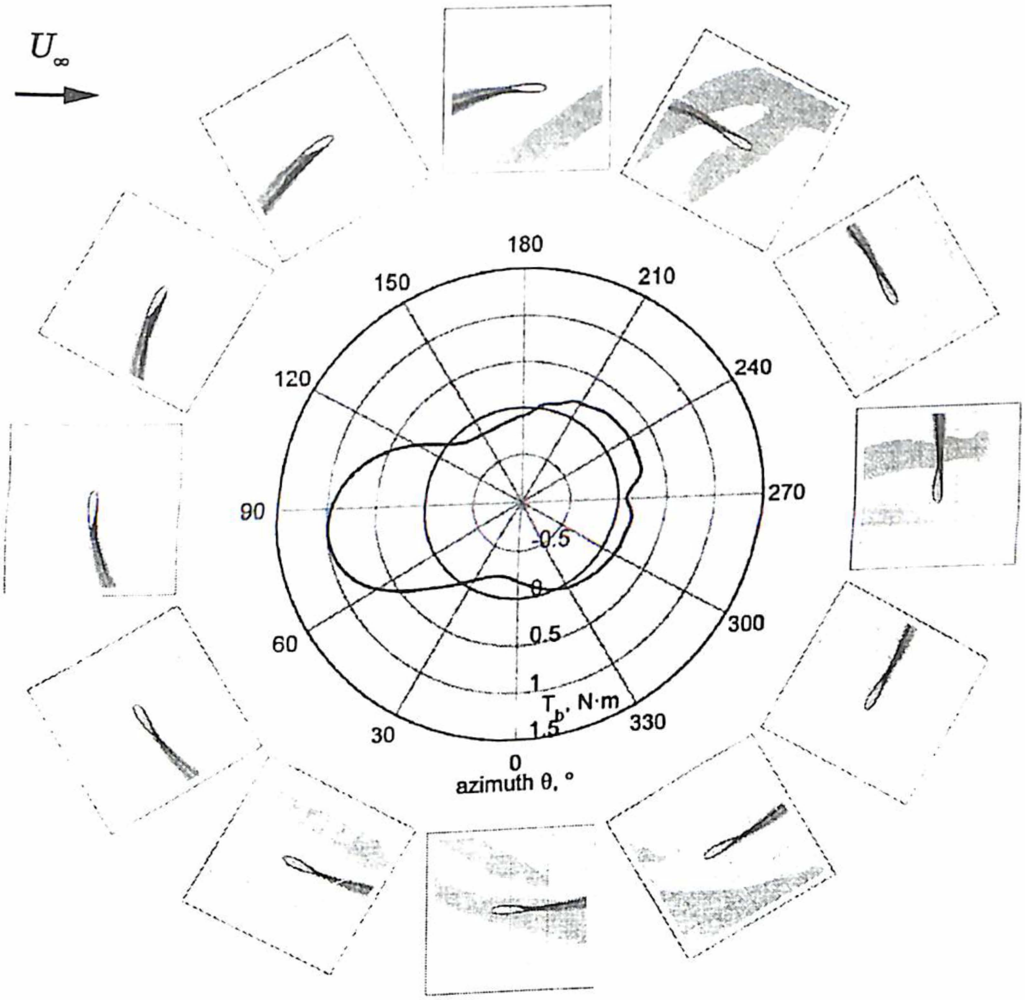

**Figure 22.** Plot showing blade torque and flow field variation with azimuth for steady wind case $U_\infty = 7m/s$ at $\lambda = 4$.

### *Flowfield at $\lambda = 4$*

In Figure 22, the variation of blade torque $T_b$ through one rotation is plotted alongside flow visualisations. Clearly $T_b$ is largely positive throughout, with notably high values from around $\theta = 60°$ up to just before $\theta = 120°$. Blade stall within this azimuth range is relatively shallow and only becomes significant after $\theta = 120°$ where negative torque is generated until the end of the upwind at $\theta = 180°$. The high values of $T_b$ in the upwind are due to the unperturbed wind and $\alpha$ near static stall that the blade sees. The generation of high torque in the upwind that reduces the downwind flow velocity results in a flat positive $T_b$ generated from $\theta = 210°$ to $\theta = 300°$ with a prominent drop at $\theta = 270°$ due to the shaft wake.

## 6. CONCLUSIONS

Numerical simulations using RANS–based CFD have been utilised to carry out investigations on the performance of a wind tunnel VAWT. Using a validated CFD model, steady wind simulations at $U_\infty = 7\text{m/s}$ were conducted and results have shown a typical performance curve prediction for this particular VAWT scale. Within the low $\lambda$ range, there is a distinct negative trough, with drag–dominated performance consistent to experimental results. Minimum CP is computed to be –0.04 at $\lambda = 2$ and positive CP is predicted to be attained at $\lambda$'s higher than 2.5. Maximum CP is 0.33 at $\lambda^* = 4.5$ and a shift in the CFD–predicted CP curve to higher $\lambda$'s is observed relative to the experimental CP profile. A closer inspection of two $\lambda$'s reveals the fundamental aerodynamics driving the performance of the VAWT. At $\lambda = 2$, the blades experience stalled flow initially from a separation bubble forming at $\theta = 60°$ with subsequent shedding of vortices alternately cast from the blade surface until reattachment occurs very much delayed beyond halfway of the rotation. The same delayed reattachment is observed as the blade completes the rotation with partial stall still visible at $\theta = 330°$. At $\lambda = 4$, blade stall is only observed in the second quadrant of rotation with the deepest stall seen at $\theta = 130°$. High values of positive blade torque $T_b$ reaching 1N·m are predicted in the upwind while most of the downwind region from $\theta = 190°$ to $\theta = 340°$ also produce positive performance that contribute to the overall positive CP of just below 0.3.

### Nomenclature

| | |
|---|---|
| c | blade chord |
| $C_d$ | drag coefficient |
| $C_l$ | lift coefficient |
| $C_m$ | moment coefficient |
| CP | power coefficient |
| $d_o$ | pressure outlet distance from VAWT axis |
| $d_s$ | side wall distance from VAWT axis |
| gr | inflation growth rate of mesh |
| k–ω SST | variant of k–ω turbulence model |
| $P_B$ | blade power (three blades) |
| $P_w$ | wind power |
| $T_b$ | blade torque (single blade) |
| Tu | turbulence intensity |
| U | instantaneous wind speed |
| $U_\infty$ | free stream wind speed |
| $y^+$ | dimensionless wall distance |

| | |
|---|---|
| $\alpha$ | angle of attack |
| $\Delta$CP | change in CP |
| $\Delta t$ | in CFD, time step size |
| $\theta$ | azimuth position |
| $\lambda$ | tip speed ratio, $R\omega/U_\infty$ |
| $\lambda^*$ | tip speed ratio at peak CP |
| $\mu$ | laminar viscosity |
| $\mu_t$ | turbulent viscosity |
| $\omega$ | rotor angular speed |
| CFD | Computational Fluid Dynamics |
| FOV | field of view |
| PIV | Particle Image Velocimetry |
| RANS | Reynolds Averaged Navier–Stokes |
| URANS | Unsteady RANS |
| VAWT | vertical axis wind turbine |

## ACKNOWLEDGEMENT

For the funding provided for this research, Mr. Danao would like to thank the Engineering Research and Development for Technology Program of the Department of Science and Technology through the University of the Philippines' College of Engineering.

## REFERENCES

1. "Climate Change 2007: The Physical Science Basis," Technical Report No. AR4, Intergovernmental Panel on Climate Change, Cambridge, United Kingdom and New York, NY, USA.
2. Department of Energy Change and Climate. Renewable Energy in 2011, June 2012, Accessed online 31 August 2012, http://www.decc.gov.uk.
3. Department of Energy Change and Climate. UK Energy in Brief 2012, July 2012, Accessed online 31 August 2012, http://www.decc.gov.uk.
4. Iida, A., Mizuno, A., and Fukudome, K., 2004, "Numerical Simulation of Aerodynamic Noise Radiated Form Vertical Axis Wind Turbines," The 18th International Congress on Acoustics, Kyoto, Japan.
5. Mertens, S., Van Kuik, G., and Van Bussel, G., 2003, "Performance of an H-Darrieus in the Skewed Flow on a Roof," Journal of Solar Energy Engineering, 125(4), pp. 433-440.
6. Ansys Inc. Fluent 13.0 Documentation, 2010.
7. Amet, E., Maitre, T., Pellone, C., and Achard, J. L., 2009, "2d Numerical Simulations of Blade-Vortex Interaction in a Darrieus Turbine," Journal of Fluids Engineering, 131(11), pp. 111103-15.
8. Consul, C. A., Willden, R. H. J., Ferrer, E., and Mcculloch, M. D., 2009, "Influence of Solidity on the Performance of a Cross-Flow Turbine " Proceedings of the 8th European Wave and Tidal Energy Conference., Uppsala, Sweden.
9. Danao, L. A., and Howell, R., 2012, "Effects on the Performance of Vertical Axis Wind Turbines with Unsteady Wind Inflow: A Numerical Study," 50th AIAA Aerospace Sciences Meeting including the New Horizons Forum and Aerospace Exposition, Nashville, Tennessee.
10. Edwards, J., Durrani, N., Howell, R., and Qin, N., 2007, "Wind Tunnel and Numerical Study of a Small Vertical Axis Wind Turbine," 45th AIAA Aerospace Sciences Meeting and Exhibit, Reno, Nevada, USA
11. Edwards, J. M., Danao, L. A., and Howell, R. J., 2012, "Novel Experimental Power Curve Determination and Computational Methods for the Performance Analysis of Vertical Axis Wind Turbines," Journal of Solar Energy Engineering, 134(3), pp. 11.
12. Hamada, K., Smith, T. C., Durrani, N., Qin, N., and Howell, R., 2008, "Unsteady Flow Simulation and Dynamic Stall around Vertical Axis Wind Turbine Blades," 46th AIAA Aerospaces Sciences Meeting and Exhibit, Reno, Nevada, USA
13. Howell, R., Qin, N., Edwards, J., and Durrani, N., February 2010, "Wind Tunnel and Numerical Study of a Small Vertical Axis Wind Turbine," Renewable Energy, 35(2), pp. 412-422.
14. Mclaren, K., Tullis, S., and Ziada, S., 2011, "Computational Fluid Dynamics Simulation of the Aerodynamics of a High Solidity, Small-Scale Vertical Axis Wind Turbine," Wind Energy, 15(3), pp. 349-361.

15. Raciti Castelli, M., Ardizzon, G., Battisti, L., Benini, E., and Pavesi, G., 2010, "Modeling Strategy and Numerical Validation for a Darrieus Vertical Axis Micro-Wind Turbine," ASME Conference Proceedings, 2010(44441), pp. 409-418.
16. Raciti Castelli, M., Englaro, A., and Benini, E., 2011, "The Darrieus Wind Turbine: Proposal for a New Performance Prediction Model Based on Cfd," Energy, 36(8), pp. 4919-4934.
17. Simão Ferreira, C. J., Bijl, H., Van Bussel, G., and Van Kuik, G., 2007, "Simulating Dynamic Stall in a 2d Vawt: Modeling Strategy, Verification and Validation with Particle Image Velocimetry Data," Journal of Physics: Conference Series, 75(1), pp. 012023.
18. Simão Ferreira, C. J., Van Brussel, G. J. W., and Van Kuik, G., 2007, "2d Cfd Simulation of Dynamic Stall on a Vertical Axis Wind Turbine: Verification and Validation with Piv Measurements," *45th AIAA Aerospace Sciences Meeting and Exhibit*, Reno, Nevada.
19. Tullis, S., Fiedler, A., Mclaren, K., and Ziada, S., 2008, "Medium-Solidity Vertical Axis Wind Turbines for Use in Urban Environments," 7th World Wind Energy Conference, St. Lawrence College, Kingston, Ontario.
20. Mcintosh, S. C., 2009, "Wind Energy for the Built Environment," Ph.D. thesis, Cambridge University, Cambridge.
21. Danao, L. a. M., 2012, "The Influence of Unsteady Wind on the Performance and Aerodynamics of Vertical Axis Wind Turbines," Ph.D. thesis, University of Sheffield, Sheffield.
22. Lee, T., and Gerontakos, P., 2004, "Investigation of Flow over an Oscillating Airfoil," Journal of Fluid Mechanics, 512(pp. 313-341.